Geophysical Journal International

Geophys. J. Int. (2015) **203,** 1726–1737
GJI Seismology

doi: 10.1093/gji/ggv395

Seismic characterization of fracture compliance in the field using *P*- and *S*-wave sources

Greg Foord,[1] James P. Verdon[2] and J-Michael Kendall[2]

[1]*BP Exploration, Chertsey Road, Sunbury, Middlesex TW*16 7*LN, United Kingdom*
[2]*School of Earth Sciences, University of Bristol, Wills Memorial Building, Queen's Road, Bristol BS*8 1*RJ, United Kingdom.*
E-mail: James.Verdon@bristol.ac.uk

Accepted 2015 September 15. Received 2015 September 14; in original form 2015 June 16

SUMMARY

Near-surface seismic field experiments using both *P*- and *S*-wave sources were carried out to image fractured limestones at two sites in southwest England. We measured *P*- and *S*-wave seismic velocities at multiple azimuths to aligned fracture sets, allowing us to determine the seismic anisotropy generated by these fractures. The effect of aligned fractures on seismic anisotropy is commonly modelled in terms of the additional compliance introduced by the fractures. Therefore, an understanding of fracture compliance is crucial both in terms of interpreting observations of anisotropy in the field and in forward modelling the effects of fractures on seismic wave propagation. Of particular concern is (1) the scaling of fracture compliance with fracture length scale, and (2) the controls on the ratio of normal to tangential compliance of the fractures ($\Omega = Z_N/Z_T$). Our experimental design allows us to image both, and we find that $\Omega = 0.37 \pm 0.06$ and $\Omega = 0.75 \pm 0.10$ for our two study sites, while the absolute values of the tangential compliance range from 0.66×10^{-11} to 5.0×10^{-11} Pa^{-1} m.

Key words: Fracture and flow; Controlled source seismology; Seismic anisotropy.

1 INTRODUCTION

Aligned fracture networks are often a major control on rock permeability. Therefore geophysical techniques that are able to image aligned fractures in the subsurface are of significant value in a range of industrial settings. Examples include petroleum migration in low-permeability rocks, water movement in hydrologic and hydrothermal systems and magma transport in volcanic systems. Of particularly timely concern is the need to monitor the movement of waste products, such as water, CO_2 and spent nuclear fuel, stored in subsurface reservoirs.

The velocities of seismic waves travelling through rock are affected by the presence of aligned fractures: velocities become direction-dependent, and in the case of *S*-waves, polarity-dependent. This situation is known as seismic anisotropy. Within industrial settings, several methods for measuring seismic anisotropy have been used to image fractures, including azimuthal variations in *P*-wave amplitudes (e.g. Hall & Kendall 2003; Duxbury *et al.* 2012) and non-hyperbolic moveout (Van der Baan & Kendall 2002; Vasconcelos & Tsvankin 2006); analysis of vertical seismic profile (VSP) data (e.g. Worthington & Hudson 2000); and observations of shear-wave splitting made on both controlled source seismic data (e.g. Wikel *et al.* 2012) and on microearthquakes induced by reservoir activities (e.g. Teanby *et al.* 2004). However, observations of anisotropy are not direct proxies for aligned fracture networks: rock physics models must be used to relate measured anisotropy to the physical mechanisms, such as aligned fractures, that have produced the anisotropy (e.g. Verdon *et al.* 2009).

Similarly, rock physics models are often used to forward model the anisotropy generated by a given fracture network (e.g. Vlastos *et al.* 2006; Sayers & den Boer 2012). Therefore in both the forward and inverse cases, a rock physics model that simulates the effects of fracture networks on seismic anisotropy is a prerequisite.

To have confidence in our models, they must be calibrated and benchmarked with measurements. Models are often calibrated in the laboratory, where the properties of the measured fractures can be constrained by the experimenter (e.g. Rathore *et al.* 1994; Tillotson *et al.* 2012; Choi *et al.* 2014). However, calibrations at the field scale, which are necessary to properly characterize scale-dependent properties, are few and far between: for most field-scale studies the properties of the fractures under investigation are not independently constrained, and therefore any attempt to calibrate a model becomes 'dangerously close to a circular argument' (Hobday & Worthington 2012).

In this paper, we perform seismic experiments on fractured rocks at or near to the surface using a hammer source and geophone arrays. Because these rocks outcrop at the surface, we have an independent characterisation of the fractures with which we can calibrate the rock physics models that link our observations of anisotropy with fracture models.

2 MODELLING OF SEISMIC ANISOTROPY

Before describing our field experiments, in this section we outline the rock physics commonly used to model how aligned fractures

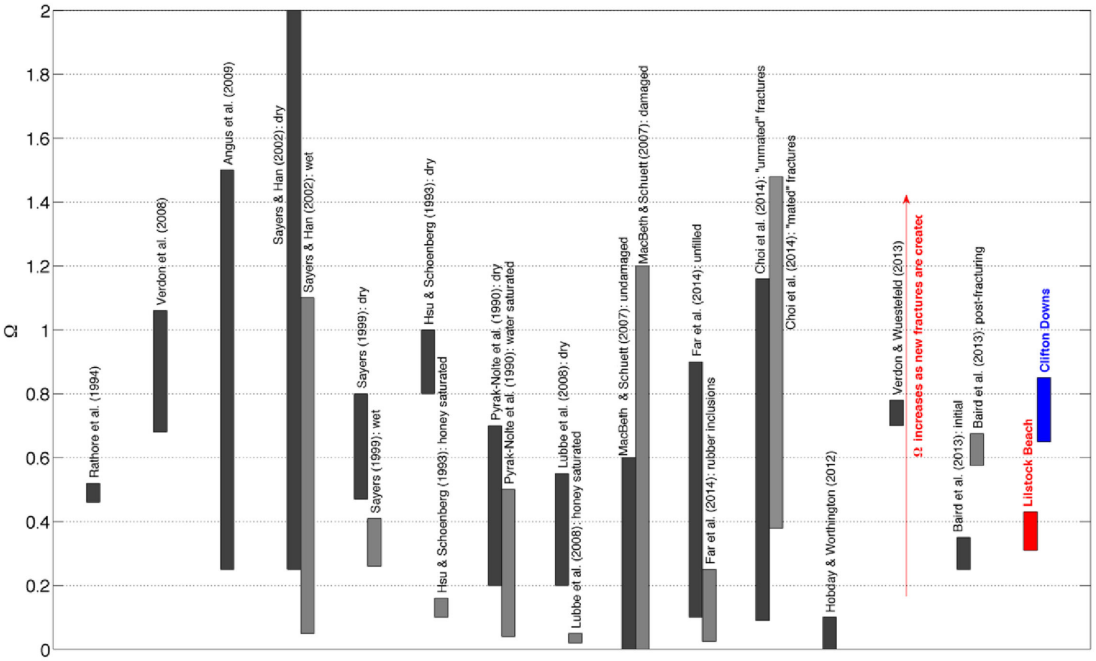

Figure 1. Compilation of Ω from the literature, with recent field studies added (modified from Verdon & Wüstefeld 2013).

affect seismic waves. When the fractures are smaller than the seismic wavelength, a fractured rock can be treated as an 'effective medium', whose elastic properties can be described by a single stiffness tensor, **C**, or its inverse, compliance tensor, **S**. **C** and **S** are both fourth-order, 3 × 3 × 3 × 3 tensors. Numerous models that simulate the effects of fractures on effective medium stiffness tensors have been developed, including Hudson (1981), Tandon & Weng (1984), Thomsen (1995), and Arts *et al.* (1996).

Probably the most commonly used modelling type is the additional compliance approach developed by Schoenberg, Sayers, and co-authors (Schoenberg 1980; Schoenberg & Douma 1988; Hsu & Schoenberg 1993; Sayers & Kachanov 1995; Schoenberg & Sayers 1995; Sayers 2002). Following this approach, the overall compliance of a fractured rock mass can be considered as the sum of the compliance of the intact, unfractured rock, $\mathbf{S}^{\mathrm{r}}$ and the additional compliance produced by the fractures, $\mathbf{\Delta S}$:

$$\mathbf{S} = \mathbf{S}^{\mathrm{r}} + \mathbf{\Delta S} \tag{1}$$

If the fractures are rotationally invariant (i.e. they are symmetric about the fracture normal) then the compliance tensor of the fracture network can be represented by two terms, Z_N and Z_T, which represent respectively the compliance of the fractures to deformation normal to the fracture faces and parallel to the fracture faces. In contracted Voigt notation, the additional compliance tensor for a fracture set aligned in the x_2–x_3 plane is:

$$\mathbf{\Delta S} = \begin{pmatrix} Z_N & 0 & 0 & 0 & 0 & 0 \\ 0 & 0 & 0 & 0 & 0 & 0 \\ 0 & 0 & 0 & 0 & 0 & 0 \\ 0 & 0 & 0 & 0 & 0 & 0 \\ 0 & 0 & 0 & 0 & Z_T & 0 \\ 0 & 0 & 0 & 0 & 0 & Z_T \end{pmatrix}. \tag{2}$$

Of particular significance is the ratio of fracture compliances Z_N/Z_T, referred to henceforth as Ω. This ratio is commonly assumed to be ≈1. However, recent studies (e.g. Hobday & Worthington 2012; Verdon & Wüstefeld 2013) have shown that Ω is in fact sensitive to the fluids filling the fractures, as well as the internal architecture of the fractures—the roughness of the fracture faces and the presence of cement bonds or detrital material filling the fractures. Measurement of Ω, in addition to measuring the absolute values of fracture compliance, represents the principal aim of our field experiments.

2.1 Controls on fracture compliance ratios

Verdon & Wüstefeld (2013) compiled measurements of Ω available in the literature. The majority of these measurements are from laboratory studies. However, the need for field studies has been recognised, and this deficiency is being addressed. In Fig. 1, we update this compilation in view of this and other recent studies that include field measurements from either near surface experiments (Hobday & Worthington 2012) or microseismic monitoring of hydraulic fracture stimulation (Baird *et al.* 2013; Verdon & Wüstefeld 2013), as well as recently published laboratory studies (Choi *et al.* 2014; Far *et al.* 2014).

Both experiments and rock physics models have shown that Ω is sensitive to both the fluid that is filling the fracture and the structure of the fracture itself. Hudson (1981) shows that for a planar, 'penny-shaped', unfilled fracture $\Omega = 1 - \nu/2$. Given that $\nu \approx 0.25$ for most sedimentary rocks, Ω will therefore be close to 1. However, adding a stiff, incompressible fluid will decrease Z_N, but leave Z_T unchanged, with the net effect of reducing Ω substantially. That is unless fluids are able to flow between fractures and 'equant' pore space during the passage of a seismic wave, then the normal compliance of the fracture will be less affected. These effects have been observed in numerous experimental studies as indicated in Fig. 1. Whether or not this flow can occur will be determined by the permeability of the formation, the viscosity of the fluid and the frequency of the incident seismic wave. This frequency-dependence leads to frequency-dependent shear-wave splitting (e.g. Al-Harrasi *et al.* 2011). Assuming a penny-shaped crack, Pointer *et al.* (2000)

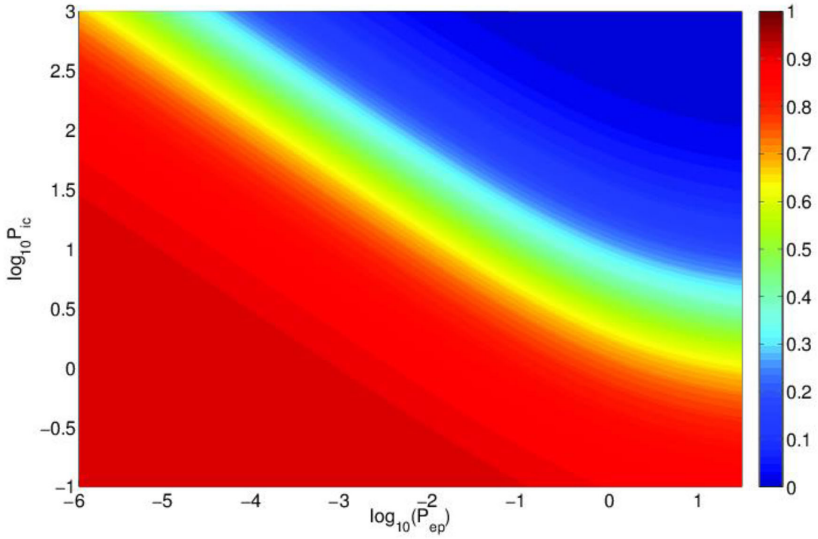

Figure 2. Ω as a function of P_{ic} and P_{ep} for a penny-shaped crack. If the fluid is soft (low P_{ic}) or can flow between fractures and the pore space (low P_{ep}) then $Z_N \approx Z_T$. Otherwise, Z_N will be smaller than Z_T. Background rock parameters of $\lambda = 8$ GPa and $\mu = 16$ GPa are used.

define a fluid incompressibility factor, P_{ic} and an equant porosity factor, P_{ep}, that influence Ω:

$$P_{ep} = \frac{2\omega\eta c^2}{\varphi\kappa K_f}, \tag{3}$$

$$P_{ic} = \frac{K_f}{a\mu}, \tag{4}$$

where ω is the frequency of the incident seismic wave, η and K_f are the viscosity and bulk modulus of the fluid filling the fracture, c and a are the aperture and aspect ratio of the fracture, ϕ, κ and μ are the porosity, permeability and shear modulus of the rock. Ω is computed from P_{ic} and P_{ep} as:

$$K = \frac{P_{ic}}{\pi}\left(\frac{\lambda + 2\mu}{\lambda + \mu}\right)\left(1 + \frac{3(1-i)}{2P_{ep}^{1/2}}\right)^{-1}, \tag{5}$$

$$\Omega = \frac{3\lambda + 4\mu}{4(\lambda + \mu)(1 + K)}, \tag{6}$$

where λ is the Lamé parameter of the rock. The impact of P_{ic} and P_{ep} on Ω is demonstrated in Fig. 2.

Ω is also sensitive to the 'internal architecture' of the fracture: the presence of asperities, rough fracture faces, and detrital infilling material for example, because fractures in reality are rarely if ever actually penny-shaped cracks (e.g. Batzle *et al.* 1980). Sayers *et al.* (2009) numerically modelled the influence that asperities in fractures have on Ω. Such effects have also been observed in both the laboratory (e.g. Choi *et al.* 2014; Far *et al.* 2014) and in the field, where both Verdon & Wüstefeld (2013) and Baird *et al.* (2013) observed increases in Ω during the course of hydraulic fracture stimulation treatments. These increases were interpreted as being caused by the creation of new, clean, open fractures overprinting pre-existing fractures that may had more asperities, detrital material and/or rougher faces.

2.2 Inversion of field measurements for fracture compliance

In the following sections we describe our field measurements of azimuthal velocity variations. In order to invert these measurements for estimates of fracture compliance, we use the method of Amadei & Savage (1993) as described by Hobday & Worthington (2012). An effective medium can be expressed in terms of the following moduli:

$$\frac{1}{E_i^{em}} = \frac{1}{E} + \frac{1}{k_{ni} D_i}, \tag{7}$$

and

$$\frac{1}{\mu_{ij}^{em}} = \frac{1}{\mu} + \frac{1}{k_{ti} D_i} + \frac{1}{k_{tj} D_j} \tag{8}$$

where E and μ are the Young's modulus and shear modulus of the intact, unfractured rock, k_n and k_t are the normal and tangential stiffnesses of individual fractures (given in units of Pa/m), and D is the fracture spacing. The subscripts i and j refer to the orthogonal orientations of the fractures (i.e. normal to the x, y and z directions). The compliance of individual fractures—the inverse of their stiffness, is given as B_N and B_T, while the compliance of the overall fracture set is denoted by $Z = B/D$. We note that this approach neglects any intrinsic anisotropy in the rock matrix due to crystal alignment (e.g. Valcke *et al.* 2006), but this is expected to be small for limestones.

These moduli described in eqs (7) and (8) can be used to construct a compliance tensor for the fractured medium:

$$\mathbf{S} = \begin{pmatrix} 1/E_x^{em} & -\nu/E & -\nu/E & 0 & 0 & 0 \\ -\nu/E & 1/E_y^{em} & -\nu/E & 0 & 0 & 0 \\ -\nu/E & -\nu/E & 1/E_z^{em} & 0 & 0 & 0 \\ 0 & 0 & 0 & 1/\mu_{yz}^{em} & 0 & 0 \\ 0 & 0 & 0 & 0 & 1/\mu_{xz}^{em} & 0 \\ 0 & 0 & 0 & 0 & 0 & 1/\mu_{xy}^{em} \end{pmatrix} \tag{9}$$

where ν is the Poisson's ratio of the unfractured rock.

Once the compliance tensor has been computed, it is inverted to give the stiffness tensor, **C**, which is used in the Christoffel equation to compute azimuthal variations in *P*- and *S*-wave velocities. We do so using the MSAT MS_phasevels function described by Walker & Wookey (2012). In each case we perform an inversion, searching for the optimum fracture compliance values that minimise the root-mean-squared (RMS) misfit between observed and modelled

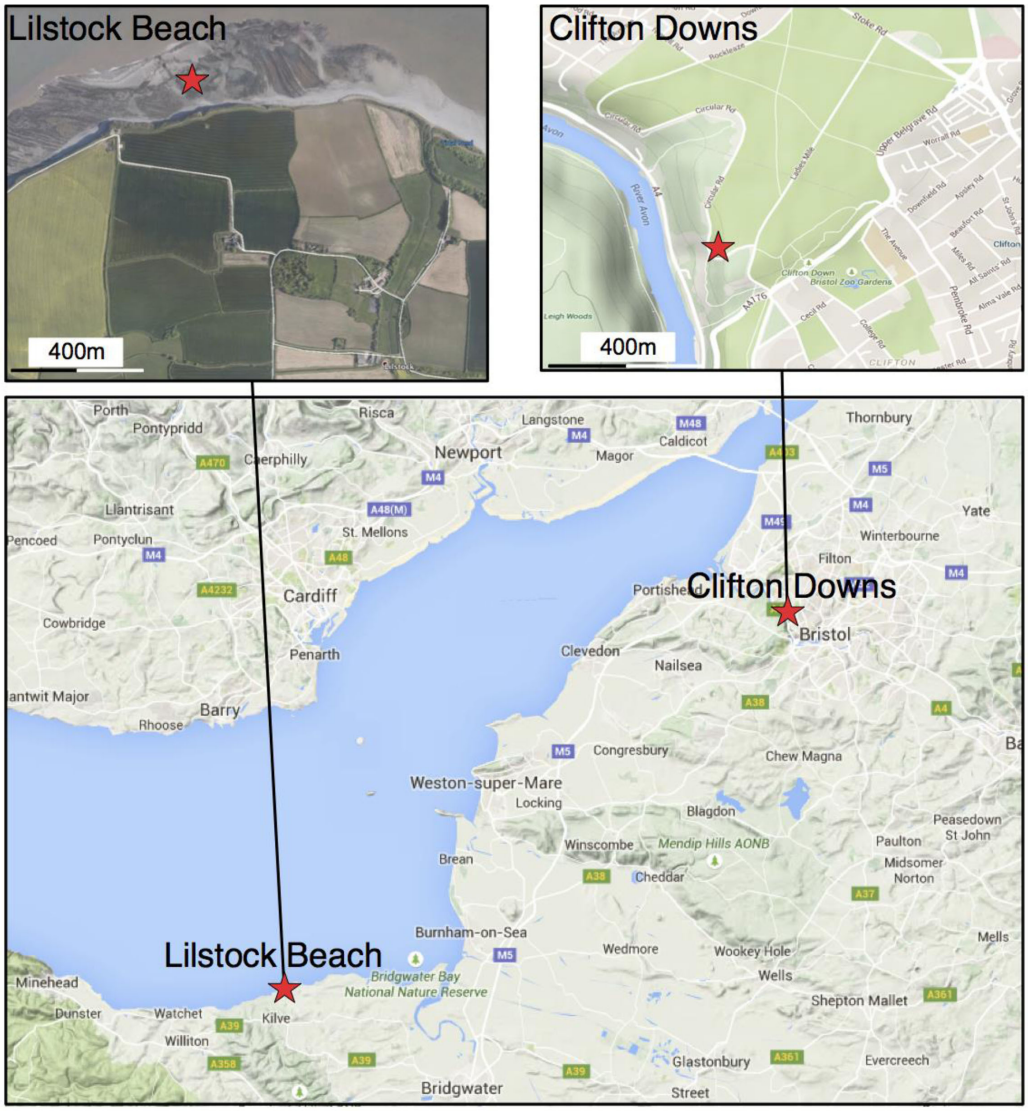

Figure 3. Locations of our study sites in SW England (images from Google). The stars indicate the locations of our experiments.

seismic velocities. We search the parameter space using the Neighbourhood Algorithm described by Sambridge (1999). 95 per cent confidence limits are computed via the diagonals of the covariance matrix of the regression parameters, which in turn are computed from the $n_o \times n_p$ Jacobian matrix computed at the best fit point (where n_o is the number of velocity observations in the inversion, and n_p is the number of parameters inverted for).

To calculate this compliance tensor requires estimates of the stiffness moduli of the unfractured rock. Ideally, independent measurements of the Young's and shear moduli would be made. However, Hobday & Worthington (2012) instead make estimates of the unfractured rock properties based on the measured velocities. Assuming that the observed traveltimes are perturbed only by the presence of two orthogonal fracture sets, the traveltimes in the x and y directions, t_x and t_y, over a distance d, will be given by:

$$t_x = \frac{d}{V_m} + N_x \delta t, \tag{10}$$

$$t_y = \frac{d}{V_m} + N_y \delta t \tag{11}$$

where V_m is the P-wave velocity of the unfractured rock, and N_x and N_y are the mean number of fractures in the x and y directions. The velocity perturbation caused by the fracture sets is described by δt, the delay in time caused across each fracture. Because δt cannot easily be measured, eqs (10) and (11) can be re-arranged to produce:

$$V_m = \frac{d(N_x - N_y)}{(N_x t_y - N_y t_x)}, \tag{12}$$

from which the unfractured rock velocity can be determined.

3 FIELD EXPERIMENTS

We perform seismic experiments at two sites in southwest England: The Clifton Downs, Bristol, and Lilstock Beach on the north Somerset coast.

3.1 Lilstock Beach

Lilstock is a small village on the north Somerset coastline (51.20°N, 3.19°W, Fig. 3). The beach underneath Lilstock is an excellent

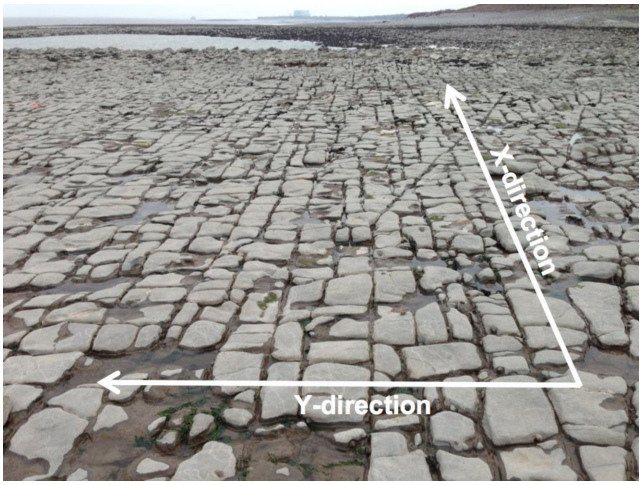

Figure 4. Lilstock Beach study location. 'x' and 'y' axes are defined parallel to the two main, orthogonal fracture sets.

Table 1. Fracture spacings measured at the Lilstock Beach site.

	x-Direction spacing (m)	y-Direction spacing (m)
Minimum	0.09	0.08
Lower quartile	0.23	0.16
Median	0.28	0.23
Upper quartile	0.33	0.28
Maximum	0.46	0.55

outcrop of the Mesozoic Blue Lias formation which consists of interbedded limestones (5–40 cm thick) and shales (up to 3 m thick) (Engelder & Peacock 2001; Belayneh & Cosgrove 2010).

The fractures at Lilstock Beach are generally contained within the limestone beds. This is to be expected because fractures typically form more readily in stiffer or more brittle layers, perpendicular to the layer boundaries. Very rarely they extend through bedding contacts into the shale layers (Engelder & Peacock 2001).

Fracturing in the limestone layers reveals a complex history of deformation that is still disputed (e.g. Rawnsley *et al.* 1998; Engelder & Peacock 2001; Belayneh 2004). However, regardless of the mechanism of formation, there are at least five sets of fractures present in the rocks at Lilstock, although not all stages are present in every limestone layer. In order to simplify our seismic experiment, we selected a wave-cut platform (at 51.20299°N, 3.19940°W) with two major orthogonal fracture sets, and a third minor set at an oblique angle. A photograph of the study location is shown in Fig. 4. We define x and y axes as parallel to the two major orthogonal fracture sets—factures aligned parallel to the x-direction have the highest fracture density. The spacing between fractures across the study area was measured by hand and is reported in Table 1.

3.2 The Clifton Downs

The Clifton Downs is an area of parkland near to the city centre of Bristol, adjacent to the Avon Gorge. The study site was located at 51.46520°N, 2.62845°W, overlooking the gorge (Fig. 3). Carboniferous limestones, known locally as the Clifton Down Limestone formation, underlie this area of the Downs. For this site, the rocks directly under investigation are buried beneath a thin layer of topsoil. However, the spacing and orientation of fractures in this unit can be investigated via their outcrops in the cliff walls of the Avon Gorge. The limestone beds dip southwards at approximately 20°, with the most obvious fracture set oriented sub-parallel to the southward strike (Hawkins 1987).

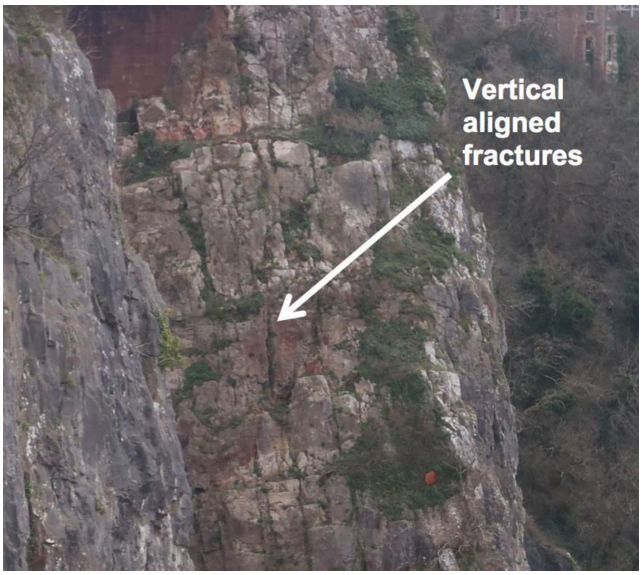

Figure 5. Photograph of the Avon Gorge cliff face (facing southwards). Southward-striking fractures are visible with spacing ≈0.5 m. The Clifton Downs study was conducted on the grassy parkland at the top of these cliffs.

A photograph of the fractures in the Avon Gorge cliff face is shown in Fig. 5. Fractures are observed to have a spacing of less than 0.5 m. However, access to these outcrops near the top of a high cliff is challenging, so this is only an estimate. Better access to this formation can be obtained via St. Vincent's Cave, but this is situated approximately 800 m to the south of our study site. This site indicates a second fracture set oriented obliquely to the main southward-striking set, with a wider spacing between fractures. Nevertheless, there is no guarantee that the fractures beneath our chosen site correspond to those observed in the cliff face; therefore these observations are merely estimates. We define x and y axes as 80° and 350° respectively: the y axis is parallel to the estimated alignment of the most obvious fracture set observed in the Avon gorge.

3.3 Data acquisition

Our study of fracture compliance broadly follows the method described by Hobday & Worthington (2012), using a hammer source to shoot near-surface refraction profiles to investigate azimuthal anisotropy. However, due to logistical differences, different strategies were used for the two different sites described above.

At Lilstock, the geophones had to be coupled to the bare rock. The usual geophone spikes were replaced with metal 'feet', which were glued to the rock using CrystalBond™ glue. This rendered the geophones immobile, so we used an array design that would enable us to measure multiple azimuths without moving the geophones. The array of 16 geophones were laid out on a 15 × 15 m^2 grid, as shown in Fig. 6. The shotpoints were placed at 5 m intervals around the grid. The P-wave velocities were calculated from the first arrival of the direct wave at each geophone—the small geometry of the array meant that no refracted phases were observed. The seismic data were measured using a Geometrics 24-channel Geode seismic recorder, and vertical-component geophones with a 10 Hz dominant frequency. A sampling rate of 0.25 ms was used and no filters were applied during processing.

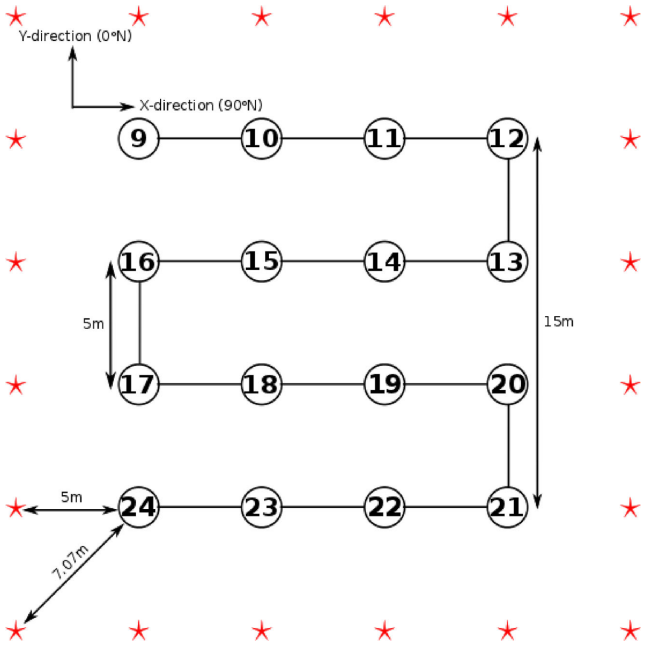

Figure 6. Schematic illustration of experiment design for Lilstock Beach. Geophones were arranged in a 15 × 15 m^2 grid with 5 m spacing between geophones (numbered circles). Shot points were placed 5 m outside the grid (red stars).

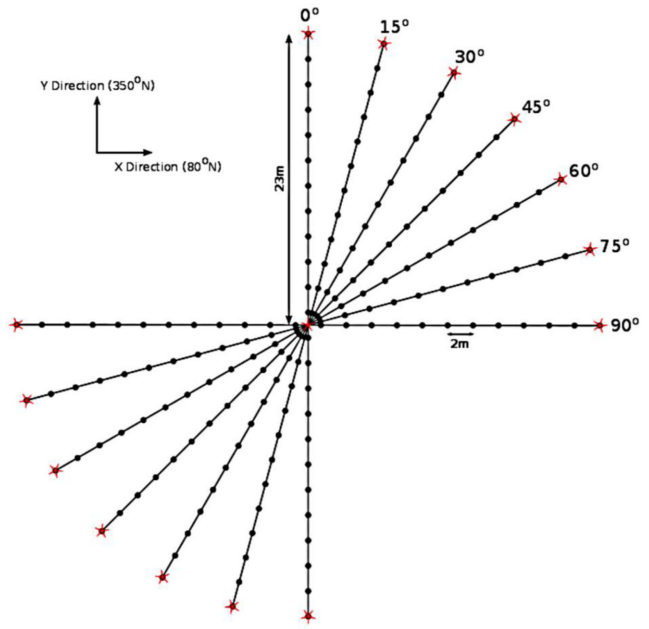

Figure 7. Schematic illustration of the experiment design for the Clifton Downs. A line of 24 geophones at 2 m spacing (black dots) was rotated by 15° intervals, with hammer shots at each end and the middle of the line (red stars). This survey design was used for both *P*- and *S*-wave experiments.

For the Clifton Downs site, geophones could be inserted into the topsoil by hand, allowing us to re-orient the array with ease. We therefore shot refraction lines with 24 geophones at 2 m spacing, with azimuthal spacing of 15° and shotpoints at either end and in the centre of each line (Fig. 7). For this site we performed both a *P*-wave survey, using the same equipment as described above, and also an *S*-wave survey using an 'anvil' *S*-wave source and single-component 4.5 Hz horizontal geophones aligned perpendicular to the seismic line in order to record the S_H component.

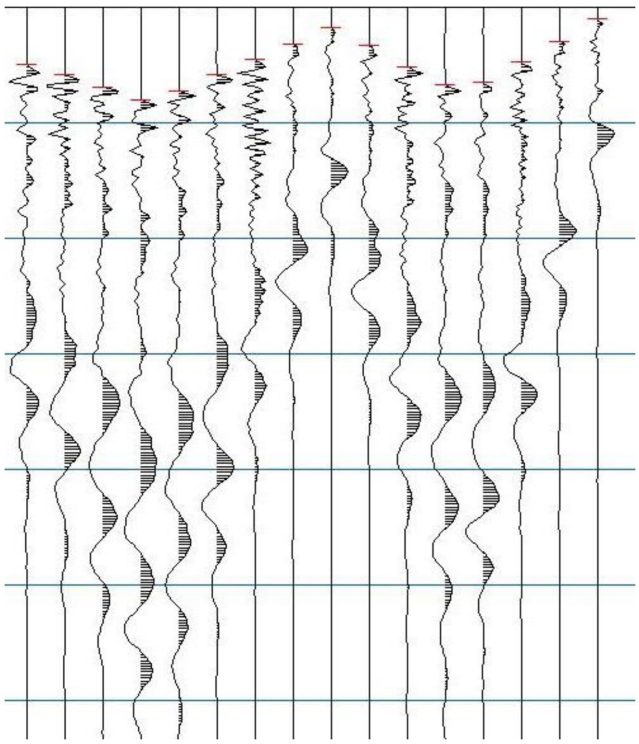

Figure 8. Raw waveform data from the Lilstock Beach experiment, showing the 16 geophone channels and the first arrival picks (red ticks). Onsets are clear and can be accurately picked.

4 RESULTS

4.1 Lilstock Beach

Fig. 8 shows an example of waveforms collected at Lilstock. Although a potential source of uncertainty for studies such as these is from picking errors, the majority of our data shows little noise, and first arrivals could usually be clearly and accurately picked. However, for the Lilstock experiment, the nearest geophones were only 5 m from the shotpoints. This short distance means that any picking discrepancy will be amplified into a significant velocity error. Inspection of the data revealed that unrealistic velocities were often recovered from these geophones, and so they were discounted from our analysis, and we restrict our analysis to data from geophones at a distance greater than 10 m from the shotpoint.

Fig. 9 shows the mean measured *P*-wave velocities at Lilstock for each measured angle from the *y*-axis defined in Section 3.1. The error bars mark 1 standard deviation of the measured velocities. The observed scatter is most likely attributable to the fact that measurements are made at the same angle across slightly different portions of rock. Our approach assumes that the effective medium is homogenous across the study area, while in reality fracture spacing varies across the outcrop, and it is likely that the properties of the fractures may also vary.

We begin by estimating the background, unfractured *P*-wave velocity using eq. (12), the mean *P*-wave velocities computed parallel to the *x*- and *y*-axes, and the median fracture spacings reported in Table 1, finding a value of 3920 m s^{-1}.

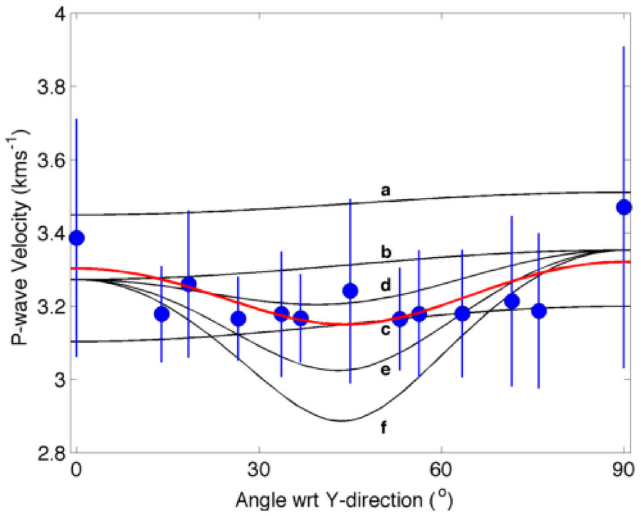

	B_N ($\times 10^{-11}$ m/Pa)	B_T ($\times 10^{-11}$ m/Pa)	Ω
a	0.15	0.15	1.0
b	0.225	0.225	1.0
c	0.31	0.31	1.0
d	0.225	0.45	0.5
e	0.225	1.125	0.2
f	0.225	2.25	0.1

Figure 9. Measured *P*-wave velocities at Lilstock Beach (blue dots) as a function of azimuth from the *y*-direction (as defined in Fig. 2). Curves labelled a–f show modelled velocities using parameters defined in the table. The red curve shows the modelled velocities for the best-fitting model.

In order to demonstrate the role of fracture compliance and Ω on azimuthal velocity variations, in Fig. 9 we show example modelling curves generated using eqs (7)–(9). Curves *a–c* represent scalar fractures where $\Omega = 1$, while curves *d–f* show the effect of increasing the tangential compliance and hence $\Omega < 1$. It is apparent that measured velocities are higher at azimuths of both 0° and 90°. This pattern can only be achieved with models that have $\Omega < 1$, implying that scalar cracks are not an adequate representation.

To find the best-fitting model, we perform an inversion to find the values of B_T and Ω that minimise the RMS misfit between measured and modelled velocities. Following Hobday & Worthington (2012), we invert for a single value of Ω to represent both fracture sets. We do this because, for the experimental setup available, it is not possible to constrain different values of Ω for the given fracture sets, as the inversion becomes underdetermined. Given that both fracture sets will have experienced similar diagenetic histories, this is a reasonable constraint to impose. Moreover, we have investigated the effects of including separate Ωs for each fracture set, but we find that this does not actually provide any improvement in the RMS misfit in comparison to using a single value of Ω for both sets.

Therefore the free parameters in our inversion are the tangential compliances of the two individual fracture sets (B_{Tx} and B_{Ty}) and a single compliance ratio (Ω). We find the best-fit model has $B_{Tx} = 6.63 \times 10^{-12} \pm 0.95\,\mathrm{m\,Pa^{-1}}$, $B_{Ty} = 5.70 \times 10^{-12} \pm 0.82\,\mathrm{m\,Pa^{-1}}$, and $\Omega = 0.37 \pm 0.06$. The red curve in Fig. 9 marks the modelled velocities generated by this best-fit model.

4.2 The Clifton Downs

Fig. 10 shows examples of the raw waveforms from the *P*- and *S*-wave experiments on the Clifton Downs. As well as a direct phase and at least two head waves can be identified (Fig. 11). Fig. 12 shows an example inversion for subsurface structure along the *x* and *y* axes of the study area (as defined in Fig. 5) This is done using modules of the commercial software suite SeisImager/2D™ (Geometrics 2009), which are used for refraction analysis. In this case we use a tomographic inversion of the first-breaks to develop a velocity models for each azimuthal profile.

These inversions confirm the presence of southward-dipping beds as observed in the outcrops of the Avon Gorge (Hawkins 1987), which serves as a preliminary quality control for our measurements. Three distinct velocity layers are identified, with *P*-wave velocities of approximately 300, 1000 and >2000 $\mathrm{ms^{-1}}$. These are interpreted respectively as topsoil; poorly consolidated, weathered rock; and intact limestone bedrock. For the remainder of this section we focus on the azimuthal velocity variations in the limestone bedrock, which are shown in Fig. 13. We again use the measured velocities parallel to the *x* and *y* axes to estimate the *P*-wave velocity of the unfractured rock via eq. (12), in this case finding a value of 4430 $\mathrm{ms^{-1}}$.

The fracture spacings, D_i in eqs (3) and (4), are not known for the Clifton Downs rocks. Therefore we instead consider the compliance of the fracture network being imaged, *Z*, rather than the compliance of individual fractures, *B*. If the fracture spacing were known, *B* could be determined from *Z*. As per Fig. 9, we show modelled curves for both scalar fractures ($\Omega = 1$) and for cases where $\Omega < 1$. The overall trend in the observed velocities is that the fastest *S*-waves are at oblique angles to either fracture set (30°–60°), while *P*-waves velocities decrease at increasing angles to the *y* axis, with the possibility that velocities are slowest at oblique angles (60°). From our modelled curves, it is again clear that models with $\Omega < 1$ do a better job of fitting the data trends than do scalar fracture models.

As per Section 4.1, we perform an inversion to find the fracture compliance values that minimise the RMS misfit between observed and measured velocities. The free parameters in the inversion are the compliances of each fracture set, Z_{Tx} and Z_{Ty}, and a single fracture compliance ratio Ω for both fracture sets. Again, we find that allowing an additional free parameter in the form of different Ω values for each fracture set does not improve the RMS misfit. For the Clifton Down experiment, we model both *P*- and *S*-wave velocities. We do not have an independent estimate for V_P/V_S ratios, so we also include the V_P/V_S ratio as an additional free parameter in our inversion.

We find that the model that minimizes RMS misfit has $Z_{Ty} = 1.0 \pm 0.14 \times 10^{-10}\ \mathrm{Pa^{-1}}$, $Z_{Tx} = 0.59 \pm 0.09 \times 10^{-10}\ \mathrm{Pa^{-1}}$, $\Omega = 0.75 \pm 0.10$, and $V_P/V_S = 1.65 \pm 0.26$. The coloured curves in Fig. 13 mark the velocities generated by this model. The compliance (Z_T) of the fracture set aligned parallel to the *y*-direction (approximately north–south) is approximately twice that of the set aligned in the *x*-direction (east–west). If we assume that both fracture sets have similar values for B_T, this implies that the fractures striking north–south are more closely spaced than those striking east-west. This matches the observations made regarding fractures in the cliffs of the Avon Gorge and St. Vincent's Cave, where the north-south striking fracture set was seen to be the main fracture set.

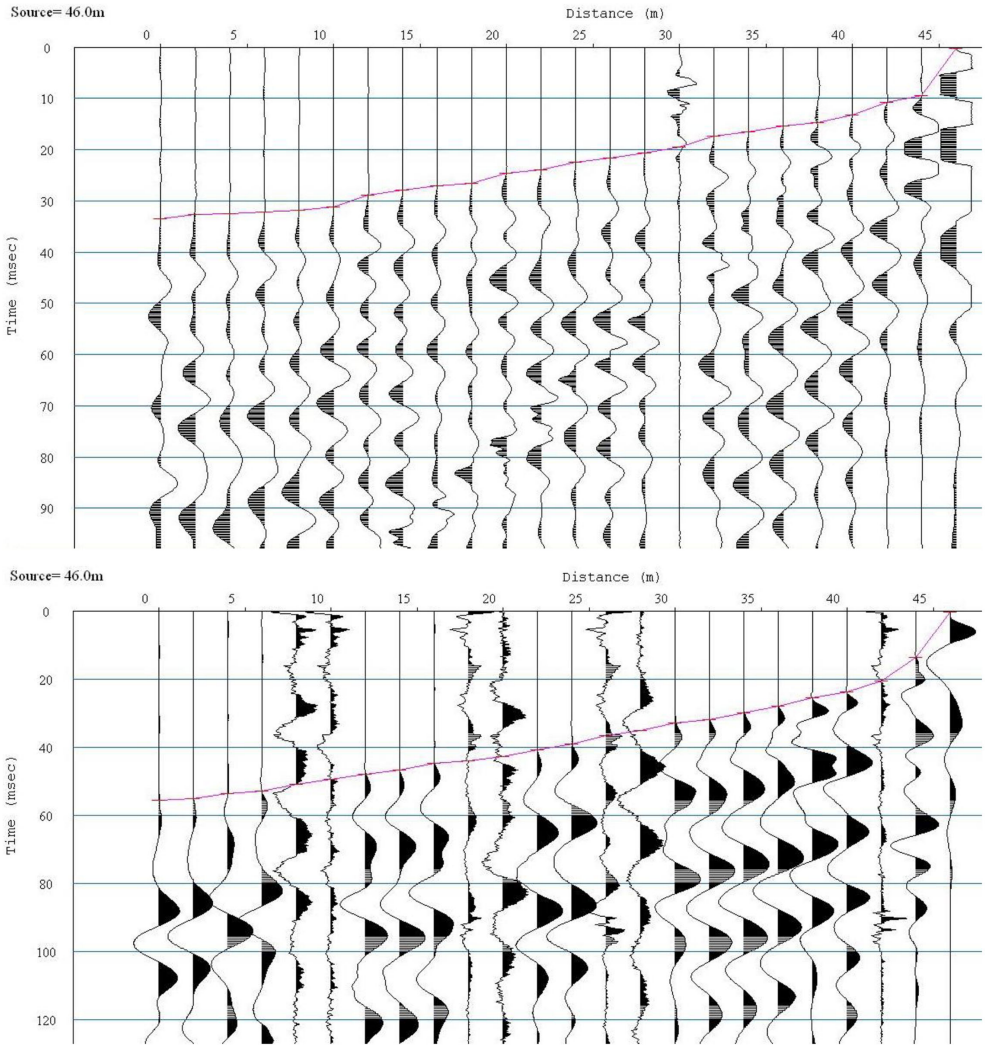

Figure 10. Raw data collected from refraction profiles on the Clifton Downs for the *P*-wave (top) and *S*-wave (bottom) surveys. Picked first arrival times are marked in pink.

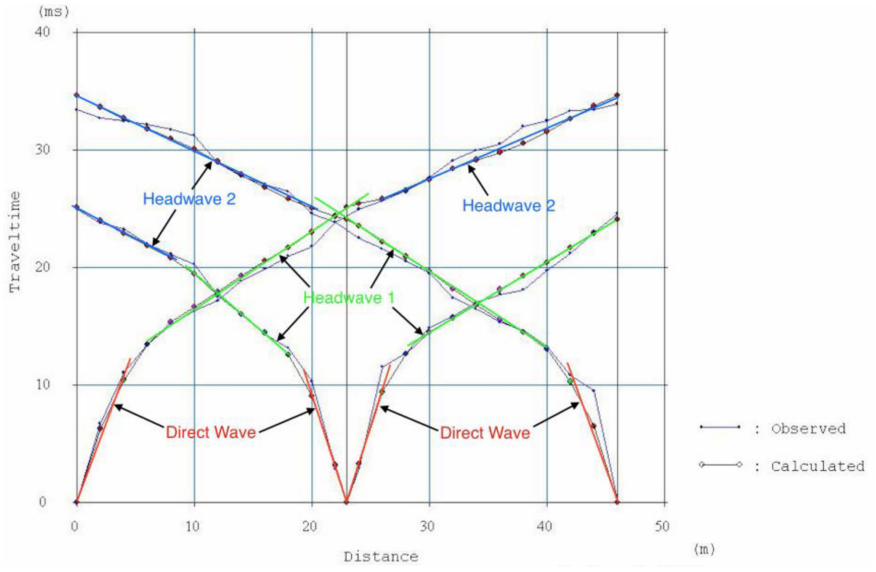

Figure 11. First-arrival time curves used to invert for subsurface structure on the Clifton Downs. A direct wave (red) and two head waves (green and blue) are fit to the observed first break traveltime picks (black dots and lines).

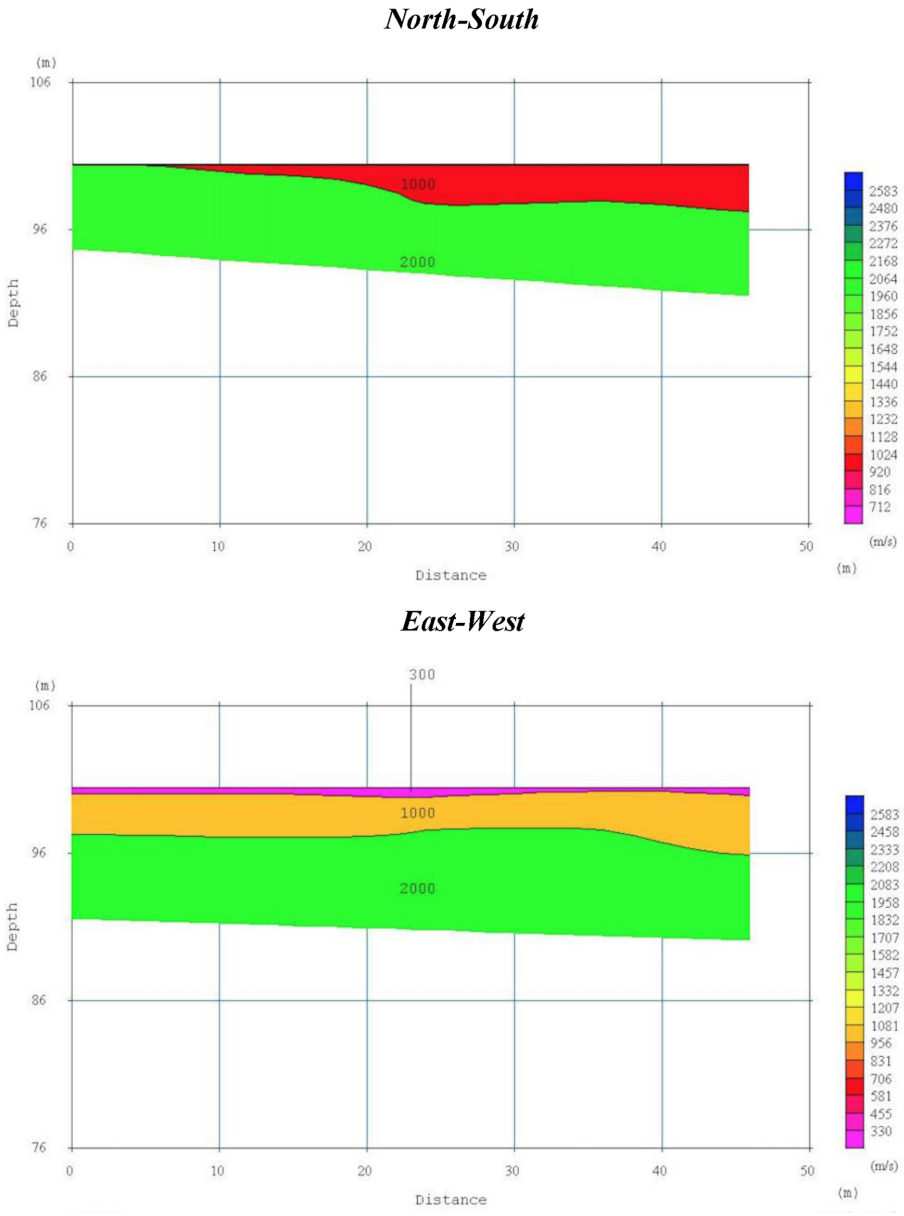

Figure 12. Inverted cross-sections from the N–S and E–W refraction profiles on the Clifton Downs. In the N–S profile, the southward-dipping beds can be seen.

5 DISCUSSION

5.1 Assessment of fit between observed and modelled velocities

For the Lilstock study, the velocities from our best-fit model fall within the error limits of the observed velocities for every propagation angle. However, for the Clifton study, our best-fit model does not satisfy the observed velocities for all propagation angles (Fig. 13). Hobday & Worthington (2012) encountered similar difficulties, and ascribe these discrepancies to lateral variations across the study area, where the inversion procedure assumes constant matrix velocity and fracture compliances, and this is likely to be the case in our studies as well. For Hobday & Worthington (2012), the trend in velocity variations with azimuth is of greater importance than individual velocity measurements. It is for this reason that we show the representative curves a–f in Figs 11 and 13.

For the Lilstock study (Fig. 11), the velocities parallel to the x and y axes are higher than those at intermediate angles. This can only be achieved by models with $\Omega < 1$ (curves d–f) because scalar crack models ($\Omega = 1$) result in velocities that increase monotonically with the angle to the y-direction (curves a–c).

For the Clifton study (Fig. 13), P-wave velocities decrease with increasing angle, with a possible minimum at $\sim 60^\circ$, while S-wave velocities are lowest when parallel to both the x and y axes, and elevated at oblique angles. Again, these velocities cannot be reproduced by scalar crack models, which produce constant S-wave velocities regardless of azimuth (curves a, b and c), whereas models with $\Omega < 1$ do produce these azimuthal S-wave velocity variations (curves d–f).

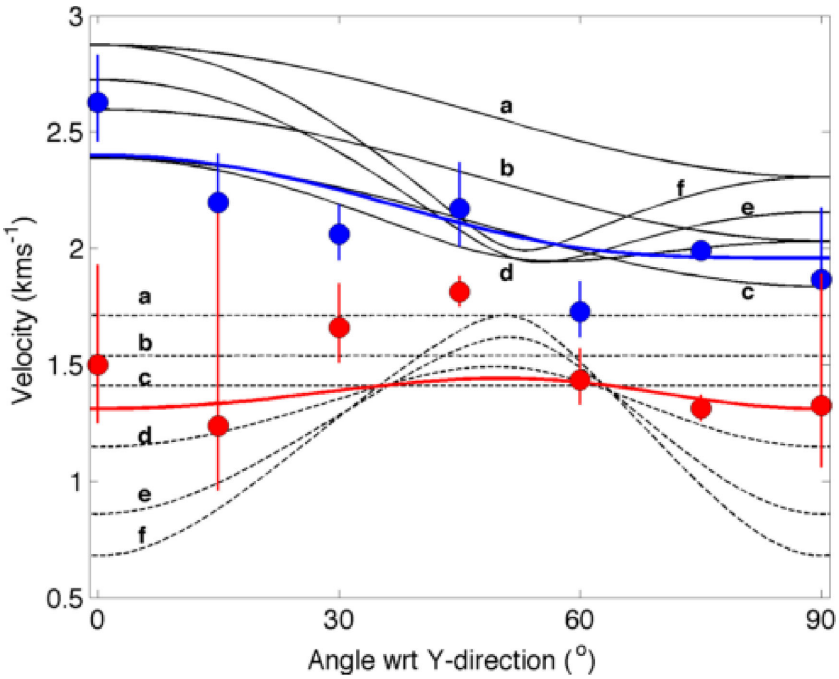

	Z_T **(x)** ($\times 10^{-11}$ Pa^{-1})	Z_T **(y)** ($\times 10^{-11}$ Pa^{-1})	**Ω**
a	5.0	2.5	1.0
b	7.0	3.5	1.0
c	9.0	4.5	1.0
d	7.0	3.5	0.5
e	6.0	3.0	0.2
f	5.0	2.5	0.1

Figure 13. Measured *P*-wave (blue dots) and *S*-wave (red dots) velocities on the Clifton Downs as a function of azimuth from the *y*-direction (as defined in Fig. 5). Curves labelled a–f show modelled *P*-wave (solid) and *S*-wave (dashed) velocities using parameters defined in the table. The blue and red curves show the modelled *P*-wave (blue) and *S*-wave (red) velocities for the best-fitting model.

5.2 Observed fracture compliances in context

The interplay between fluid effects and fracture architecture effects mean that determining a single cause for changes in Ω can be challenging. Nevertheless, the values of Ω obtained for Lilstock Beach and the Clifton Downs are within the typical ranges expected. The value of Ω measured at Lilstock Beach is lower than that obtained for the Clifton Downs. The Lilstock Beach site is submerged at high tide—our measurements were made a few hours after high tide, once the wave-cut platform was exposed. It is therefore likely that the fractures were at least partially saturated with water. The fractures on the Clifton Downs are less likely to be water-saturated: the surveys were performed on days with dry weather, and the position of the survey site on top of the Avon Gorge cliffs means that the rocks analysed, which are only a few metres below the surface (Fig. 12), are unlikely to be below the water table. This difference in saturation may account for the differences in Ω between the Lilstock Beach and Clifton Downs sites. However, it may simply be that differences in the internal architecture of the fractures can account for these observations.

Worthington & Lubbe (2007) investigated the relationship between fracture lengths and compliance. Fig. 14 shows a compilation of measurements from the literature, along with our results. For the Clifton Downs experiment, we have inverted for Z rather than B because the fracture spacing has not been measured directly. We therefore estimate B assuming a fracture spacing of 0.5 m, as inferred from observations of fractures seen in the cliffs of the Avon Gorge. The fractures measured in our field areas have variable lengths. Following Hobday & Worthington (2012) we plot our results at a fracture dimension of 10 m, which is a somewhat arbitrary representation of the scales of fractures measured. Our measurements of fracture compliance fit well within the scaling relationship between fracture compliance and fracture length established by Worthington & Lubbe (2007).

6 CONCLUSIONS

We have performed near-surface seismic experiments at two sites in the UK to measure the compliance of fracture networks. We have measured both the absolute tangential compliance of the fractures (B_T), and the normal-to-tangential compliance ratio, Ω. A better understanding of these parameters is important both to improve efforts to numerically model wave propagation through fractured media, as well as to use observations of seismic anisotropy to characterise fracture networks in a range of settings, including water aquifers, oil and gas reservoirs, and even magma systems. Furthermore, such analysis provides valuable parameters for geomechanical modelling of fractured reservoirs (e.g. Angus *et al.* 2010).

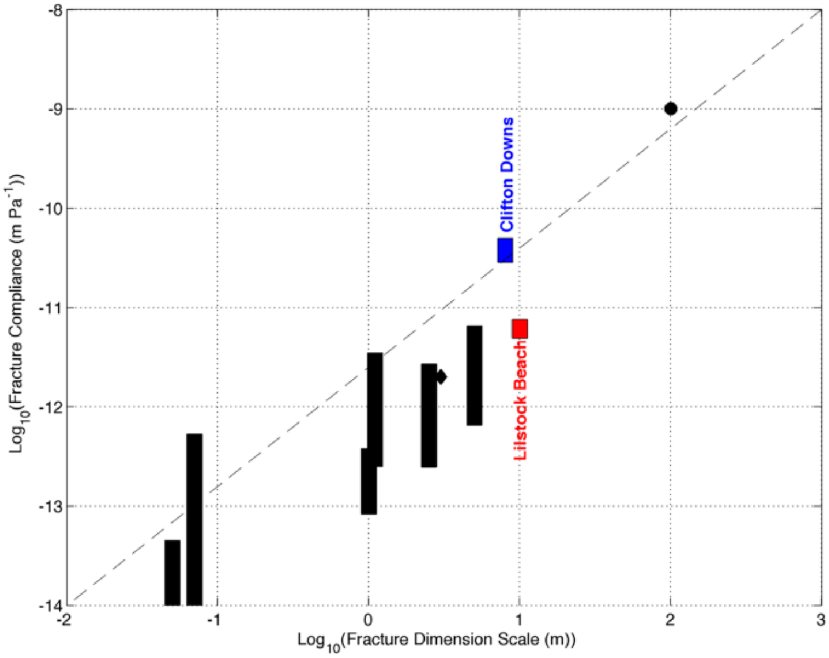

Figure 14. Compilation of measurements of fracture compliance as a function of fracture size. Modified from Verdon & Wüstefeld (2013).

Future work could focus on the affect of fluid types on compliance ratios. For example, it would be worth making repeat measurements at Lilstock, both before and after high-tide, and using horizontal-component (*S*-wave) geophones in addition to vertical-component (*P*-wave) geophones. Temporal changes in Ω (e.g. Baird *et al.* 2013; Verdon & Wüstefeld 2013) can be used to track fluid migration and fracture network development.

We find values for B_T and Ω that fit with previous observations from a range of settings. It is also important to note that these experiments give an order-of-magnitude estimate of fracture size, and reveal the orientation (strike) of the dominant fracture set.

ACKNOWLEDGEMENTS

The authors thank Terradat UK Ltd. for providing them with the *S*-wave source and geophones. Both JMK and JPV are funded by the British Geological Survey.

REFERENCES

Al-Harrasi, O.H., Kendall, J.-M. & Chapman, M., 2011. Fracture characterization using frequency-dependent shear wave anisotropy analysis of microseismic data, *Geophys. J. Int.,* **185,** 1059–1070.

Amadei, B. & Savage, W.Z., 1993. Effect of joints on rock mass strength and deformability, in *Comprehensive Rock Engineering,* pp. 361–365, ed. Hudson, J.A., Pergamon.

Angus, D.A., Verdon, J.P., Fisher, Q.J. & Kendall, J.-M., 2009. Exploring trends in microcrack properties of sedimentary rocks: an audit of dry core velocity-stress measurements, *Geophysics,* **74,** E193–E203.

Angus, D.A., Kendall, J.-M., Fisher, Q., Segura, S., Crook, A. & Dutko, M., 2010. Modelling microseismicity of a producing reservoir from coupled fluid-flow and geomechanical simulation, *Geophys. Prospect.,* **58,** 901–914.

Arts, R.J., Rasolofosaon, P.N.J. & Zinszner, B.E., 1996. Experimental and theoretical tools for characterizing anisotropy due to mechanical defects in rocks under varying pore and confining pressures, in *Seismic Anisotropy,* pp. 384–432, eds Fjaer, E., Holt, R.M. & Rathore, J.S., Society of Exploration Geophysics.

Baird, A.F., Kendall, J.-M., Verdon, J.P., Wuestefeld, A., Noble, T.E., Li, Y., Dutko, M. & Fisher, Q.J., 2013. Monitoring increases in fracture connectivity during hydraulic stimulations from temporal variations in shear wave splitting polarization, *Geophys. J. Int.,* **195,** 1120–1131.

Batzle, M.L., Simmons, G. & Siegfried, R.W., 1980. Microcrack closure in rocks under stress: direct observation, *J. geophys. Res.,* **85,** 7072–7090.

Belayneh, M., 2004. Palaeostress orientation inferred from surface morphology of joints on the southern margin of the Bristol Channel Basin, UK, in *The Initiation, Propagation, and Arrest of Joints and Other Fractures,* pp. 243–255, eds Cosgrove, J.W. & Engelder, T., Geological Society of London Special Publications 231.

Belayneh, M. & Cosgrove, J.W., 2010. Hybrid veins from the southern margin of the Bristol Channel Basin, UK, *J. Struct. Geol.,* **32,** 192–201.

Choi, M.-K., Bobet, A. & Pyrak-Nolta, L.J., 2014. The effect of surface roughness and mixed-mode loading on the stiffness ratio κ_X/κ_Z for fractures, *Geophysics,* **79,** D319–D331.

Duxbury, A., White, D., Samson, C., Hall, S.A., Wookey, J. & Kendall, J.-M., 2012. Fracture mapping using seismic amplitude variation with offset and azimuth analysis at the Weyburn CO_2 storage site, *Geophysics,* **77,** N17–N28.

Engelder, T. & Peacock, D.C.P., 2001. Joint development normal to regional compression during flexural-flow folding: the Lilstock buttress anticline, Somerset, England, *J. Struct. Geol.,* **23,** 259–277.

Far, M.E., de Figueiredo, J.J.S., Stewart, R.R., Castagna, J.P., Han, D.-H. & Dyaur, N., 2014. Measurements of seismic anisotropy and fracture compliances in synthetic fractured media, *Geophys. J. Int.,* **197,** 1845–1857.

Geometrics, 2009. '*SeisImager/2D*™ *Manual, Version 3.3*'. Available at: ftp://geom.geometrics.com/pub/seismic/SeisImager/Installation_CD/SeisImager2D_Manual/SeisImager2D_Manual_v3.3.pdf, last accessed 16 June 2015.

Hall, S.A. & Kendall, J.-M., 2003. Fracture characterization at Valhall: application of *P*-waves amplitude variation with offset and azimuth (AVOA) analysis to a 3D ocean-bottom data set, *Geophysics,* **68,** 1150–1160.

Hawkins, A.B., 1987. The cliff face under the Clifton suspension bridge, Avon Gorge, Bristol, *Q. J. Eng. Geol. Hydrogeol.,* **20,** 2–4.

Hobday, C. & Worthington, M.H., 2012. Field measurements of normal and shear fracture compliance, *Geophys. Prospect.,* **60,** 488–499.

Hsu, C.-J. & Schoenberg, M., 1993. Elastic waves through a simulated fractured medium, *Geophysics,* **58,** 964–977.

Hudson, J.A., 1981. Wave speeds and attenuation of elastic waves in material containing cracks, *Geophys. J. R. astr. Soc.,* **64,** 133–150.

Lubbe, R., Sothcott, J., Worthington, M.H. & McCann, C., 2008. Laboratory estimates of normal and shear fracture compliance, *Geophys. Prospect.,* **56,** 239–247.

MacBeth, C. & Schuett, H., 2007. The stress dependent elastic properties of thermally induced microfractures in aeolian Rotliegend Sandstone, *Geophys. Prospect.,* **55,** 323–332.

Pointer, T., Liu, E. & Hudson, J.A., 2000. Seismic wave propagation in cracked porous media, *Geophys. J. Int.,* **142,** 199–231.

Pyrak-Nolte, L.J., Myer, L.R. & Cook, N.G.W., 1990. Transmission of seismic waves across single natural fractures, *J. geophys. Res.,* **95,** 8617–8638.

Rathore, J.S., Fjaer, E., Holt, R.M. & Renlie, L., 1994. *P*- and *S*-wave anisotropy of a synthetic sandstone with controlled crack geometry, *Geophys. Prospect.,* **43,** 711–728.

Rawnsley, K.D., Peacock, D.C.P., Rives, T. & Petit, J.-P., 1998. Jointing in the Mesozoic sediments around the Bristol Channel Basin, *J. Struct. Geol.,* **20,** 1641–1661.

Sambridge, M., 1999. Geophysical inversion with a neighbourhood algorithm – 1. Searching a parameter space, *Geophys. J. Int.,* **138,** 479–494.

Sayers, C.M., 1999. Stress-dependent seismic anisotropy of shales, *Geophysics,* **64,** 93–98.

Sayers, C.M., 2002. Stress-dependent seismic anisotropy of sandstones, *Geophys. Prospect.,* **50,** 85–95.

Sayers, C.M. & den Boer, L.D., 2012. Characterizing production-induced anisotropy of fractured reservoirs having multiple fracture sets, *Geophys. Prospect.,* **60,** 919–939.

Sayers, C.M. & Han, D.-H., 2002. The effect of pore fluid on the stress-dependent elastic wave velocities in sandstones, *SEG Expanded Abstracts,* **21,** 1842–1845.

Sayers, C.M. & Kachanov, M., 1995. Microcrack-induced elastic wave anisotropy of brittle rocks, *J. geophys. Res.,* **100,** 4149–4156.

Sayers, C.M., Taleghani, A.D. & Adachi, J., 2009. The effect of mineralization on the ratio of normal to tangential compliance of fractures, *Geophys. Prospect.,* **57,** 439–446.

Schoenberg, M., 1980. Elastic wave behavior across linear slip interfaces, *J. acoust. Soc. Am.,* **68,** 1516–1521.

Schoenberg, M. & Douma, J., 1988. Elastic wave propagation in media with parallel fractures and aligned cracks, *Geophys. Prospect.,* **36,** 571–590.

Schoenberg, M. & Sayers, C.M., 1995. Seismic anisotropy of fractured rock, *Geophysics,* **60,** 204–211.

Tandon, G.P. & Weng, G.J., 1984. The effect of aspect ratio of inclusions on the elastic properties of unidirectionally aligned composites, *Polym. Compos.,* **5,** 327–333.

Teanby, N., Kendall, J.-M., Jones, R.H. & Barkved, O., 2004. Stress-induced temporal variations in seismic anisotropy observed in microseismic data, *Geophys. J. Int.,* **156,** 459–466.

Thomsen, L., 1995. Elastic anisotropy due to aligned cracks in porous rock, *Geophys. Prospect.,* **43,** 805–829.

Tillotson, P., Sothcott, J., Best, A.I., Chapman, M. & Li, X.-Y., 2012. Experimental verification of the fracture density and shear-wave splitting relationship using synthetic silica cemented sandstones with a controlled fracture geometry, *Geophys. Prospect.,* **60,** 516–525.

Valcke, S., Casey, M., Lloyd, G., Kendall, J.-M. & Fisher, Q., 2006. Seismic anisotropy in sedimentary rocks, *Geophys. J. Int.,* **166,** 652–666.

Van der Baan, M. & Kendall, J.-M., 2002. Estimating anisotropy parameters and traveltimes in the tau-p domain, *Geophysics,* **67,** 1076–1086.

Vasconcelos, I. & Tsvankin, I., 2006. Non-hyperbolic moveout inversion of wide-azimuth *P*-wave data for orthorhombic media, *Geophys. Prospect.,* **54,** 535–552.

Verdon, J.P. & Wüstefeld, A., 2013. Measurement of the normal/tangential compliance ratio (Z_N/Z_T) during hydraulic fracture stimulation using *S*-wave splitting data, *Geophys. Prospect.,* **61,** 461–475.

Verdon, J.P., Angus, D.A., Kendall, J.-M. & Hall, S.A., 2008. The effects of microstructure and nonlinear stress on anisotropic seismic velocities, *Geophysics,* **73,** D41–D51.

Verdon, J.P., Kendall, J.-M. & Wüstefeld, A., 2009. Imaging fractures and sedimentary fabrics using shear wave splitting measurements made on passive seismic data, *Geophys. J. Int.,* **179,** 1245–1254.

Vlastos, S., Liu, E., Main, I.G., Schoenberg, M., Narteau, C., Li, X.-Y. & Maillot, B., 2006. Dual simulations of fluid flow and seismic wave propagation in a fractured network: effects of pore pressure on seismic signature, *Geophys. J. Int.,* **166,** 825–838.

Walker, A.M. & Wookey, J., 2012. MSAT – a new toolkit for the analysis of elastic and seismic anisotropy, *Comput. Geosci.,* **49,** 81–90.

Wikel, K., Kendall, R., Bale, R., Grossman, J. & De Meersman, K., 2012. 4D-3C geomechanical study of *in-situ* bitumen recovery in NW Canada using Toe-to-Heel Air Injection, *First Break,* **30,** 55–65.

Worthington, M.H. & Hudson, J.A., 2000. Fault properties from seismic Q, *Geophys. J. Int.,* **143,** 937–944.

Worthington, M.H. & Lubbe, R., 2007. Fractured Reservoirs: the scaling of fracture compliance, *Geol. Soc. Lond. Special Publication,* **270,** 73–82.